Extreme Value Analysis of Ground Magnetometer Observations at Valentia Observatory, Ireland

Alexandra Ruth Fogg, C. M. Jackman, J. Malone-Leigh, P. T. Gallagher, A. W. Smith, M. Lester, M. -T. Walach, J. E. Waters

AGU ADVANCING EARTH AND SPACE SCIENCES

Space Weather®

RESEARCH ARTICLE
10.1029/2023SW003565

Extreme Value Analysis of Ground Magnetometer Observations at Valentia Observatory, Ireland

Alexandra Ruth Fogg[1], C. M. Jackman[1], J. Malone-Leigh[1], P. T. Gallagher[1], A. W. Smith[2], M. Lester[3], M.-T. Walach[4], and J. E. Waters[5]

[1]School of Cosmic Physics, DIAS Dunsink Observatory, Dublin Institute for Advanced Studies, Dublin, Ireland, [2]Department of Mathematics, Physics and Electrical Engineering, Northumbria University, Newcastle upon Tyne, UK, [3]School of Physics and Astronomy, University of Leicester, Leicester, UK, [4]Physics Department, Lancaster University, Bailrigg, UK, [5]Aix Marseille University, CNRS, CNES, LAM, Marseille, France

Key Points:

- More extreme Valentia observations are observed in the premidnight sector
- Return values of extreme Valentia observations at given return periods are predicted
- Geomagnetic storms contribute more extremes than substorms or sudden commencements

Supporting Information:

Supporting Information may be found in the online version of this article.

Correspondence to:

A. R. Fogg,
arfogg@cp.dias.ie

Citation:

Fogg, A. R., Jackman, C. M., Malone-Leigh, J., Gallagher, P. T., Smith, A. W., Lester, M., et al. (2023). Extreme value analysis of ground magnetometer observations at Valentia observatory, Ireland. *Space Weather*, *21*, e2023SW003565. https://doi.org/10.1029/2023SW003565

Received 22 MAY 2023
Accepted 12 JUL 2023

Abstract Understanding global space weather effects is of great importance to the international scientific community, but more localized space weather predictions are important on a national level. In this study, data from a ground magnetometer at Valentia Observatory is used to characterize space weather effects on the island of Ireland. The horizontal component of magnetometer observations and its time derivative are considered, and extreme values of these are identified. These extremes are fit to a generalized extreme value distribution, and from this model return values (the expected magnitude of an observation within a given time window) are predicted. The causes of extreme values are investigated both in a case study, and also statistically by looking at contributions from geomagnetic storms, substorms, and sudden commencements. This work characterizes the extreme part of the distribution of space weather effects on Ireland (and at similar latitudes), and hence examines those space weather observations which are likely to have the greatest impact on susceptible technologies.

Plain Language Summary Space weather describes the effects of the interaction between the Sun's solar wind and the Earth's magnetic field, and can have dramatic impacts on human technology. Space weather can be characterized both globally, and on a local level. In this study, space weather over the island of Ireland is characterized using an Irish ground based magnetometer at Valentia Observatory. Magnetometers record a measure of the magnetic field, and these changes will be large when space weather effects are enhanced. Extreme observations from this magnetometer are detected, and these are used to predict future extreme observations. Additionally, the contributions of different types of space weather phenomena to extreme observations are determined. Understanding extreme observations on a national level will help to enhance space weather resilience which is increasingly important as society becomes more and more dependent on technology.

1. Introduction

Ground based magnetometers measure deflections in the magnetic field as a result of changes in overhead currents, which can be used to infer variations in geomagnetically induced currents (GICs, Blake et al., 2016, 2018), geoelectric fields (Campanyà et al., 2019; Malone-Leigh et al., 2023), and the overhead currents themselves (e.g., auroral electrojet indices, Davis & Sugiura, 1966). Ground based magnetometers have been used for over a century to characterize space weather effects. As the amount of data recorded at stations builds up over time, a wealth of information can be unraveled from these expanding datasets using new and/or more computationally intensive data analysis techniques (such as machine learning approaches (e.g., James et al., 2021; Marangio et al., 2020), numerical techniques (e.g., Elvidge, 2020) and visualizations (e.g., Chapman et al., 2020)).

Space weather impacts a breadth of human technology, and some technology is more susceptible than others. For example, recently 38 starlink satellites were lost to a minor-moderate size geomagnetic storm (Fang et al., 2022), while infrastructure like power grids are more robust to all but the most extreme events (Bolduc, 2002). As we move to an increasingly technologically-reliant society, these space weather risks become of greater importance, and indeed space weather is listed on national risk registers in, for example, the United Kingdom (HM Government Cabinet Office, 2020). Therefore the motivation for understanding, and indeed predicting the most extreme space weather events is of the utmost importance.

In this study, observations from an Irish magnetometer station will be characterized using Extreme Value Analysis (EVA) (e.g., Coles, 2001). By using this technique, extreme observations will be identified, and after fitting a model, return values of these extreme observations will be extracted. These return values describe the value that is expected to be observed at least once in a given return period. Characterization of return values enables understanding of what is (or indeed, isn't) an extreme observation, and how regularly these might occur. Understanding this is a fundamental part of interpreting space weather at Irish latitudes, and in relation to specific Irish geology.

Although it is not routinely used in space science, EVA is used more commonly in other fields to predict the return periods of for example, earthquakes or extreme weather (e.g., Finkel et al., 2023). EVA has also been used by some authors to predict the return period or probability of extreme Space Weather events. A limitation of the technique is the fitting of a model to detected extremes: a large amount of data is needed to result in a large number of extremes for the fitting. For example, Siscoe (1976) extracted the three largest events from each solar cycle in 91 years of aa index, and calculated statistical characteristics for the extreme values. Subsequently, Silbergleit (1996) identified sudden storm commencements (SSCs) between 1957 and 1980, and by fitting a Gumbel distribution predicted that a |Dst| value above 400 nT would be observed within the 17 ($\pm$3) years that followed 1980. Similarly, Silbergleit (1999) utilized the aa index between 1868 and 1992 (124 years), separating between odd and even solar cycles to account for Hale cycle affects. They predicted that a geomagnetic event equaling the March 1989 event (e.g., Bolduc, 2002) would occur within the next 8 odd or 13 even solar cycles.

Koons (2001) determined return values using 66 years of geomagnetic index Ap, as well as proton and electron fluxes. Additionally, Tsubouchi and Omura (2007) identified geomagnetic storms from 44 years of Dst data, and calculated that the return period of an event such as the March 1989 storm is approximately 60 years. Riley and Love (2017) also detected storms in the Dst index, and by fitting a power law estimated the probability of extreme events in Dst. Recently, Elvidge (2020) used EVA on aa index data, which spans 150 years; they first removed a strong solar cycle variation from the data using a Hilbert-Huang transform, and then predicted return values with periods up to 1,000 years, separating data into solar cycle minimum and maximum. Bergin et al. (2023) performed EVA on Dst, SYM-H, and SMR and compared the differences between the return values of these similar indices. These analyses can provide answers toward understanding one of the key questions in the field of space weather: when will the next dramatic space weather event be?

Similarly to this study, Thomson et al. (2011) estimated return values at magnetometer stations across Europe, including Irish station Valentia (51.93°N, 349.75°E geographic, with data from 1995 to 2010). Despite only using 15 years of data to fit the model, they estimated 100 and 200 years return values of both the horizontal component of the magnetic field and its time derivative. From their Figures 5 and 6, they predict a 100 years return value of 2,000 nT for H and 1,000 nT min^{-1} for $\frac{dH}{dt}$. Rogers et al. (2020) takes a similar approach, and examines trends with latitude and magnetic local time (MLT). Uniquely in this study, a larger amount of data will be used. Additionally, unlike these previous papers, an in depth analysis of one station will be presented, including specific return values, and an investigation of the causes of extreme values.

Finally, the causes of high values at an Irish magnetometer station will be investigated by considering the contributions of storms, substorms and sudden commencements (SCs). Geomagnetic storms are generated when solar wind - magnetosphere coupling is strong and prolonged; this results in enhancements in geomagnetic activity, and ultimately the storm itself. Geomagnetic storms are characterized by three phases (e.g., Hutchinson, Wright, & Milan, 2011; McPherron, 1995; M.-T. Walach & Grocott, 2019): initial, main, and recovery. During the main phase, a large amount of energy is deposited in the ring current, leading to a characteristic decrease in the ring current index, SYM-H.

Following the onset of magnetic reconnection at the dayside, open magnetic flux is pulled across the polar cap and builds up in the magnetotail. As a result, the magnetotail flares and presents a larger surface area to the solar wind, increasing the pressure within the magnetotail. This increased pressure cannot be maintained and magnetic reconnection begins in the magnetotail, resulting in a large deposition of energy into the nightside ionosphere, and effects are seen across a range of phenomena including ionospheric convection (e.g., Bristow & Jensen, 2007; Bristow et al., 2001, 2003), field-aligned currents (FACS, e.g., Sangha et al., 2020), aurorae (e.g., Nishimura et al., 2020), auroral kilometric radiation (e.g., Waters et al., 2022), and increased magnetic activity (Freeman et al., 2019). First characterized by McPherron (1970), substorms are generally divided into three phases: growth, expansion and recovery, and exhibit intense variability of the phenomena listed above.

Sudden commencements (SCs, Araki, 1994) are swift compressions of the Earth's magnetosphere driven by rapid increases in solar wind dynamic pressure known as pressure pulses. A characteristic step change signature is seen in the ring current index SYM-H (e.g., Araki, 1994; Gillies et al., 2012; Hori et al., 2015) as a result of an increase in the geomagnetic field in the equatorial plane. In this paper, SCs are divided into two phases: "onset" defines from the start of the step change in SYM-H (as detected by an event list described later) to the end of the step change. The "height" phase is then the period 10 min after the end of the step change. SCs effects span the magnetosphere-ionosphere system, and can include ULF waves (e.g., Oliveira et al., 2020) and enhancements in ionospheric convection/aurorae/FACs (e.g., Fogg et al., 2023). SCs can be further divided into events rapidly followed by a geomagnetic storm, known as SSCs, and those not followed by a storm, known as sudden impulses (SIs). For the purpose of this study, only the duration of the SC increase and the 10 min that follow will be considered. Although some differences are seen between SSCs and SIs by for example, Smith et al. (2019, 2021), this will not affect answering the question of whether SCs can drive extreme events in magnetometer observations.

2. Data

2.1. Magnetometer Data

The Magnetometer Network of Ireland (MagIE, https://www.magie.ie/), includes stations across the island of Ireland, and has been used to model the effects of GICs (Blake et al., 2016, 2018) and geoelectric fields (Campanyà et al., 2019; Malone-Leigh et al., 2023). Most recently, Malone-Leigh et al. (2023) used the MagIE network to nowcast geoelectric fields. Of course, MagIE is one of many magnetometer networks across the world, and the Valentia station in the southwest of Ireland (51.93°N, 349.75°E geographic) is a contributing station to the INTERMAGNET network (Love & Chulliat, 2013), which itself contributes to the SuperMAG data set (Gjerlov, 2012). In this study, data from the MagIE Valentia station is used, as it provides a broad parameter space of two solar cycles; data from 1991 to 2021 is extracted via the SuperMAG interface at 1 minute resolution.

Key to this study is the horizontal component of the magnetic field, B, which is calculated using Equation 1:

$$B = \sqrt{N^2 + E^2} \tag{1}$$

from the magnetic north (N) and magnetic east (E) components of the magnetic field observations. The rate of change of the horizontal component, $\frac{dB}{dt}$, is also calculated similarly to Smith et al. (2019) using Equation 2:

$$\frac{dB}{dt} = \frac{\sqrt{[N(t+dt) - N(t)]^2 + [E(t+dt) - E(t)]^2}}{dt} \tag{2}$$

where N and E are as defined previously, and dt is the time elapsed between measurements at t and $t + dt$. Both B and $\frac{dB}{dt}$ are calculated at 1 min resolution.

2.2. Event Lists

In order to compare predicted return values with geomagnetic phenomena, event lists of these phenomena are utilized, which will be described here. The geomagnetic storm list compiled by M.-T. Walach and Grocott (2019) is used in this manuscript to compare storm time values to the predicted return values. Storms are detected in a manner similar to that of Hutchinson, Wright, Milan, Grocott, and Boakes (2011), by searching for a characteristic shape in SYM-H observations. In this manuscript, 314 geomagnetic storms from this list are utilized from 1991 to 2019 inclusive, as this overlaps with Valentia data availability described above. The effects of geomagnetic storms captured by this list has been studied extensively (e.g., Orr et al., 2023; Sandhu et al., 2021; Wharton et al., 2020).

In this manuscript the Substorm Onsets and Phases From Indices of the Electrojet (SOPHIE, Forsyth et al., 2015) substorm list is used to identify substorm phases in Valentia data. The SOPHIE detection algorithm identifies characteristic substorm signatures in SML, the SuperMAG equivalent of the lower envelope of the auroral electrojet index. Two additional processing steps are applied to the SOPHIE event list to produce a list of individual substorms with three phase start times, in a similar sense to Waters et al. (2022). First, any expansion phase onsets which may be attributed to steady magnetospheric convection are removed; this is flagged directly in the event list. Second, individual substorms with growth directly followed by expansion and recovery phase are extracted;

all other identified phases are removed. This results in over 26,000 substorms being extracted from the 75% EPT (Expansion Percentile Threshold) list, covering 1996–2014. Similarly to the M.-T. Walach and Grocott (2019) storm list, the SOPHIE list has been used extensively to study the effects of substorms on the terrestrial magnetosphere (e.g., Waters et al., 2022).

Additionally, a list of SCs is compiled by the Observatori de l'Ebre (hereafter OE events, Observatori de l'Ebre, 2020). In this study, 432 positive SCs between 1995 and 2020 inclusive are extracted from the OE event list, and used to characterise to what extent SCs contribute to extreme observations. This window gives a broad parameter space of two solar cycles. The OE event detection algorithm searches for rapid variations in the traces of magnetometer stations at roughly equatorial latitude (≈33°N). Any increase with a gradient of at least 3 nT min^{-1} is recorded as an SC. This event list was commissioned by the International Association of Geomagnetism and Aeronomy, and is part of its International Service of Geomagnetic Indices, and has been used by authors to characterise the propagation of SC effects through the magnetosphere (e.g., Fogg, 2021; Fogg et al., 2023; Gillies et al., 2012).

2.3. IMF, Solar Wind, Geomagnetic Indices and Sunspot Number

Finally, upstream observations and geomagnetic indices are extracted from the OMNI (King & Papitashvili, 2005; Weimer et al., 2002, 2003; Weimer & King, 2008) data set to analyze the causes of an example extreme observation in B. All these data are retrieved from OMNIWeb (https://omniweb.gsfc.nasa.gov/hw.html) at 1 min resolution. The B_Z and B_Y components are used to characterize the interplanetary magnetic field (IMF), along with the solar wind dynamic pressure (P_{SW}), proton density (N_{SW}) and solar wind velocity (V_{SW}). Additionally, geomagnetic indices SYM-H, PC_N, AE, AU and AL are retrieved from OMNIWeb. The ring current index SYM-H is provided by the World Data Center for Geomagnetism Kyoto (Iyemori, 1990) and is derived from near equatorial latitude magnetometer stations; SYM-H shows signatures characteristic of geomagnetic storms. Analogous to SYM-H, SuperMAG index SMR (Newell & Gjerloev, 2012) is derived from all available magnetometer stations between −50° and +50° geomagnetic latitude. Similarly, the auroral electrojet indices (AE, AU, and AL, World Data Center for Geomagnetism Kyoto et al., 2015; Davis & Sugiura, 1966) are derived from auroral latitude magnetometer observations and demonstrate activity in the auroral zone; AL shows characteristic substorm signatures. SuperMAG equivalents SME, SMU, and SML (Newell & Gjerloev, 2011) are also used in this manuscript, which are derived from all available magnetometer stations between 40° and 80° geomagnetic latitude. The polar cap index PC_N (provided by the World Data Center for Geomagnetism, Copenhagen, Troshichev & Andrezen, 1985; Troshichev et al., 1979; Stauning, 2013) is derived from the variation in the trace of a polar latitude magnetometer and information from the solar wind and IMF variability; PC_N is an indicator of the speed of flux transport across the polar cap. Finally, sunspot numbers are used to characterize the solar cycle; these are obtained from Sunspot Index and Long-term Solar Observations (SILSO) at the Royal Observatory of Belgium (2020).

3. Extreme Value Analysis

In this manuscript, *Extreme Value Theory* is used to both extract extreme events from Valentia observations, and then use these events, fitting to a model, to estimate the return values of Valentia observations. This analysis will be called "EVA" in the text, and will allow quantification of the baseline conditions at Valentia. This allows understanding of what is, or indeed isn't, an unusually elevated value at the station, and indeed at similar stations at this latitude. In turn, this will enhance interpretation of magnetometer observations at this latitude, allowing characterization of whether an event is unusual. Indeed, this work will describe the likelihood of extreme events within a given time frame, and characterize the rarity of previous events at Irish latitudes.

To conduct the EVA, the python package pyextremes (Bocharov, 2023) is used, along with the package emcee (Foreman-Mackey et al., 2013) for Markov Chain Monte Carlo (MCMC) fitting (qualitatively better fits to extremes were found using MCMC fitting than maximum likelihood estimate fitting). pyextremes is used to extract the extremes, fit them to a model (described below) using emcee (used previously by Smith et al., 2018), and use the fitted model to predict return values. Unlike in Elvidge (2020), in this paper the Valentia B and $\frac{dB}{dt}$ data are not corrected for solar cycle variations before the EVA is performed. When B and $\frac{dB}{dt}$ were plotted along

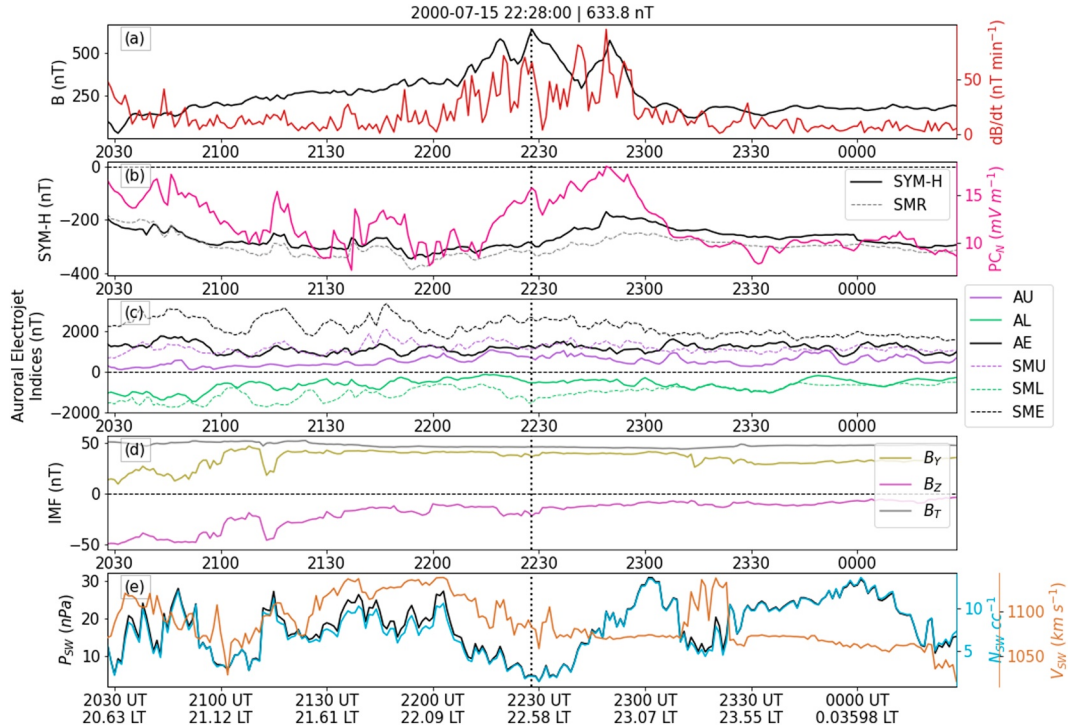

Figure 1. Timeseries of (a) Valentia B (black) and $\frac{dB}{dt}$ (red) (b) SYM-H (black), SMR (gray/dashed) and PC_N (pink) (c) auroral electrojet indices (solid) and SuperMAG equivalents (dashed) (d) interplanetary magnetic field (IMF) B_Y (yellow) and B_Z (purple) components, with total IMF magnitude $B_T = \sqrt{B_X^2 + B_Y^2 + B_Z^2}$ (gray) (e) solar wind pressure (black), proton density (blue) and solar wind velocity (gold). Centered on the detected B extreme at 22:28 UT on 15/07/2000, vertical dashed line indicates this time in all panels. The universal time is indicated on all axis ticks, and for panel (e) the magnetic local time of Valentia is also indicated.

with sunspot number (see Figure S1 in Supporting Information S1), no significant deviation from the mean with solar cycle was observed. This may be a result of only having roughly two solar cycles of Valentia data, or indeed due to the particularly weak recent solar cycle. Therefore it was deemed that the EVA could be performed on the data directly, without removing solar cycle variations. It is important to note that because the data spans a broad parameter space of two solar cycles, the results may be applicable to both past and future events.

3.1. Detecting Extremes

The first stage of the EVA is to detect extremes from the data set, ensuring that the data used to fit the model are independent and identically distributed as required for EVA. In this manuscript extremes are detected using the block maxima method (as opposed to peaks over threshold, to avoid user bias in choosing a threshold). Similarly to Elvidge (2020), the data are divided into calendar years, and the highest observation within that calendar year is detected as an extreme value; note that full calendar years of Valentia data are used from 1991 to 2021, including years with any operational data gaps. The effect of the chosen block size (i.e., calendar year in this case) on the distribution of the detected extremes was tested. For three different block sizes (calendar year, 180 days, and 90 days) the distribution of the detected extremes was plotted. The distributions were very similar across all block sizes, even though more extremes are detected for shorter block sizes. Since the distribution of extremes was the same across different block sizes, a calendar year was chosen as the block size for this study as it will capture the full cycle of ionospheric seasonality, and therefore a broad parameter space of observations. Extremes are detected in this manner for both B, and $\frac{dB}{dt}$.

First, an example of an extreme in Valentia B observations will be presented. In Figure 1, the third highest B extreme (the highest with continuous IMF and plasma data) is presented across a variety of geomagnetic indices and IMF and plasma data. In panel 1(a), Valentia B and $\frac{dB}{dt}$ observations are presented in black and red respec-

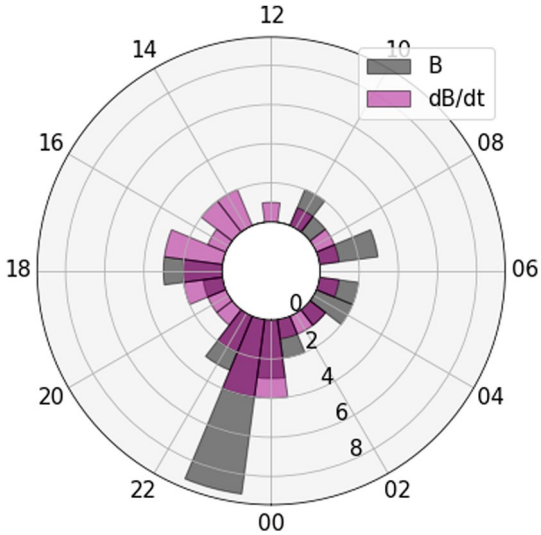

Figure 2. Histogram of the number of detected extremes with respect to the magnetic local time (MLT) of the Valentia magnetometer at the time of detection. Bins are 1 hr MLT in width, and are centered on each hour of MLT; radial length of the bar indicates the amount of extremes detected in that bin. Dark gray for extremes in B, purple for extremes in $\frac{dB}{dt}$.

tively. B comes to a peak of 634 nT at 22:28 UT on 15th July 2000, with smaller peaks shortly before and after. Interestingly, $\frac{dB}{dt}$ comes to a local peak about 20 minutes later, although the detected extreme for that year occurs at 14:48 UT on the same day. Indeed, in 43.75% (14 in 31) of calendar years investigated, the detected B and $\frac{dB}{dt}$ extreme occur within 1 day of each other. This suggests that these extremes may be driven by some shared driver, perhaps a geomagnetic storm.

Presented in panel 1(b), the ring current index SYM-H is well below the quiet level of −15 nT described by M.-T. Walach and Grocott (2019), and reaches below −200 nT at the time of the peak; this likely indicates an ongoing geomagnetic storm. SMR is similar to SYM-H in this interval. PC_N is highly elevated above the average values of 0.79 mV m^{-1} (Fogg et al., 2022), reaching beyond 15 mV m^{-1}. This indicates strong polar electrodynamics, and likely rapid transport of magnetic flux antisunwards across the polar cap. Although no obvious substorm signatures are present in AL (green curve in panel 1(c)), all of the auroral electrojet indices are highly elevated above average values (66 nT for AU, and −77 nT for AL (Fogg et al., 2022)), indicating strong activity in the auroral zone and potentially bright auroral emission. Given the strong driving in the interval, it is possible that the auroral oval has expanded beyond the range of magnetometers contributing to AE/AU/AL, so SuperMAG indices SME/SMU/SML are included as they cover a larger range in latitude. For all three indices comparisions (e.g., AE vs. SME etc), the traditional auroral electrojet index is underestimating the value of the auroral electrojet as measured by SuperMAG indices (as characterized statistically by Bergin et al., 2020). However the interpretation in this interval is similar: strong driving in the auroral zone with no clear substorm signatures.

IMF B_Y (yellow) and B_Z (purple) are presented in panel 1(d), along with the total IMF magnitude ($B_T = \sqrt{B_X^2 + B_Y^2 + B_Z^2}$, gray). At the start of the interval, IMF B_Z is strongly southwards, with values reaching −50 nT, while B_Y has a slightly lower magnitude, but is strongly positive. Although the balance of B_Z and B_Y changes, and B_Y becomes dominant, there is strong negative B_Z throughout the interval. This suggests that there is strong solar wind - magnetosphere coupling at the subsolar point in the form of magnetic reconnection, resulting in a large amount of energy being communicated into the magnetosphere. Additionally, the solar wind dynamic pressure, which is presented in panel 1(e), varies greatly throughout the interval, sometimes exceeding 25 nPa (over 10 times the average of 1.83 nPa presented by Fogg et al. (2022)). The pressure curve is dominated by the shape of the proton density (blue in panel 1(e)), which sometimes exceeds 10 cc^{-1}, over double average values presented by Fogg et al. (2022). Finally, the solar wind velocity is also highly elevated, sometimes exceeding 1,100 km s^{-1}, over double average values of 439 km s^{-1} presented by Fogg et al. (2022).

Combining these observations, it is clear that in the lead up to the observed extreme, the magnetosphere is being strongly driven by negative B_Z, with a strong B_Y component (B_Y has also been shown to increase reconnection rates by altering the position of the reconnection site (e.g., Grocott et al., 2003, 2004, 2008)), and high solar wind dynamic pressure resulting in a compressed magnetosphere. This results in storm activity in the ring current index SYM-H (strongly negative) and enhanced activity in polar and auroral electrodynamics, although this may not be directly driven by the solar wind. Additionally, it is important to note that the Valentia station is around 23 MLT at the time this extreme is observed; the MLT dependence of the observed extremes will be examined next.

A histogram of the extremes detected in both B and $\frac{dB}{dt}$ with respect to the MLT of the Valentia station at detection time is presented in Figure 2 (B extremes in gray, $\frac{dB}{dt}$ extremes in purple). For both B and $\frac{dB}{dt}$, more extremes are detected in the premidnight sector than elsewhere, although the difference is particularly stark for B. This may relate to Valentia being in the region where substorm onset is most often occurs. However, $\frac{dB}{dt}$ changes may also

be driven by step changes relating to compressional wave propagation through the magnetosphere, for example, as a result of SCs (e.g., Araki, 1994; Fogg et al., 2023; Hori et al., 2015); this may be why more $\frac{dB}{dt}$ extremes are seen at dayside MLTs than for B.

The effect of selected block size on the MLT distribution of extremes was investigated. Histograms displaying the distribution of B and $\frac{dB}{dt}$ extremes in MLT were created across three different block sizes (calendar year, 180 days, and 90 days). For B extremes, the distribution was a very similar shape for all three block sizes, with a clear spike in the premidnight sector. For $\frac{dB}{dt}$, similar to Figure 2, the distributions didn't have a clear spike near midnight, rather a spread of larger numbers of extremes between 14 MLT and 00 MLT in the dusk side magnetosphere.

3.2. Modeling the Distribution of B Extremes

Having extracted the extremes using the block maxima method described above, these are used to fit a *Generalized Extreme Value Distribution* (GEVD). The GEVD is defined in terms of:

$$G(x) = \exp\left(-1\left[1+\xi\left(\frac{x-\mu}{\sigma}\right)\right]^{-\frac{1}{\xi}}\right) \tag{3}$$

using the same notation as Elvidge (2020), where μ is the location parameter, σ is the scale parameter, and ξ is the shape parameter. The model is fitted using MCMC fitting as implemented in the emcee python package; for full details, the reader is directed to Foreman-Mackey et al. (2013).

In the limit where ξ goes to 0, the GEVD distribution becomes the Gumbel distribution:

$$G(x) = \exp\left(-\exp\left[-\frac{x-\mu}{\sigma}\right]\right) \tag{4}$$

with parameters defined as for Equation 3. pyextremes automatically selects between the GEVD and Gumbel distributions depending on which fits the data better. Best fit is characterized using the Akaike Information Criterion (AIC, Akaike, 1974): whichever distribution has the smaller AIC is chosen as it has a more optimal fit.

Figure 3 presents several ways of assessing the fit of the GEVD distribution for the B extremes. First, in panel 3(a), the observed extremes are plotted as a function of their return period (triangles), with the modeled extremes overplotted as an orange curve, with 95% confidence interval as a gray shade. The model fits the data best where there are most observed extremes: at the lower end of the y axis. However, around 20–40 years return period, the fit of the model strays away from the data. Overall, this suggests that the model is better at predicting the lower extremes, that is, those with lower return periods; this will be independent of block size, since the distribution of extremes is.

In panel 3(b), the probability distribution functions for the observed and modeled extremes are compared, with observations in gray and the model in orange. The model follows the general shape of the observed distribution, but does not reach the same peak as the observations, and over/under estimates in areas, particularly toward higher B. Note the location, scale and shape parameters are recorded on this panel for repeatability. Finally, the distributions of observed and modeled B are compared in a quantile-quantile (or QQ) plot, allowing examination of the relative shape of the distributions. For each observed extreme B, the modeled B of the same probability is extracted, and these two B values are plotted against each other. Where the values lie on the y = x line, the distributions agree, otherwise, they differ. In some places, the points lie on or very close to the y = x line, but as the distributions extend to higher B (where there are less observed extremes), the model differs from the observations. Again, this suggests that the model is better at predicting the lower extremes, likely as that is where more observations are seen.

The fitted GEVD model is then used to predict return values (this is similar to reading off the y value of the orange curve as a function of return period in panel 3(a)). These predicted return values are presented in

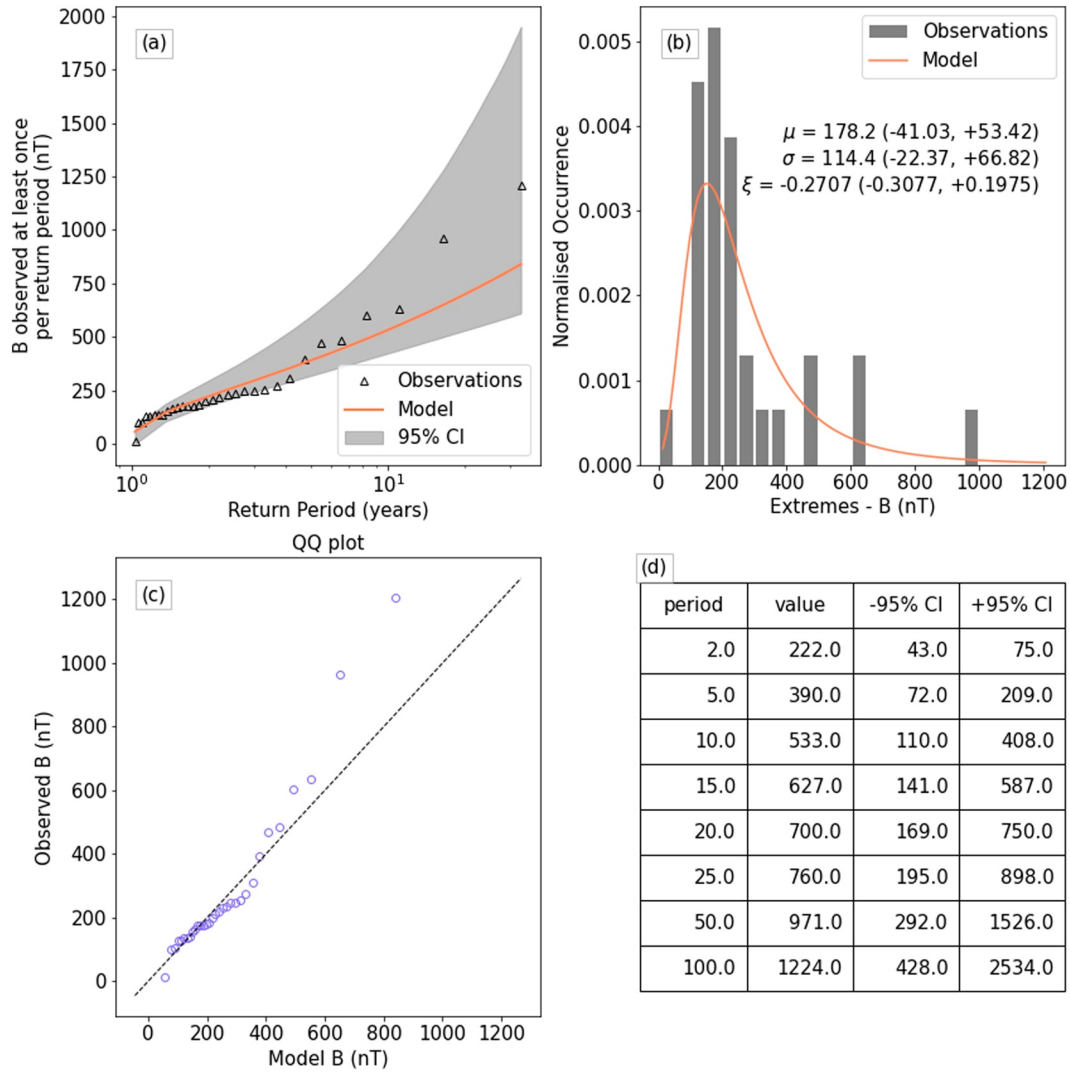

period	value	-95% CI	+95% CI
2.0	222.0	43.0	75.0
5.0	390.0	72.0	209.0
10.0	533.0	110.0	408.0
15.0	627.0	141.0	587.0
20.0	700.0	169.0	750.0
25.0	760.0	195.0	898.0
50.0	971.0	292.0	1526.0
100.0	1224.0	428.0	2534.0

Figure 3. Extreme value analysis for B. (a) Observed extremes as a function of their calculated return periods (triangles), modeled extremes as a function of return period (orange line) with 95% confidence interval (gray shade). (b) Normalized distributions of the detected B extremes (gray bars) and the fitted Generalized Extreme Value Distribution model (orange line), with the fitted parameters defined as for Equation 3 noted in the top right and the width of a 95% confidence interval. (c) Quantile-quantile plot comparing the distributions of the modeled (x) and observed (y) extremes. (d) Return values ("value") as a function of return period ("period" in years), with the width of a 95% confidence interval as an errorbar.

Figure 3d as a function of return period, and with 95% confidence interval widths recorded. Return values describe the magnitude of B which is expected to be exceeded at least once within the associated return period. For example, Valentia B observations are expected to exceed 700 nT (95% CI: −169, +750) at least once in a 20 year period.

3.3. Modeling the Distribution of dB/dt Extremes

The fitting of the GEVD model to the $\frac{dB}{dt}$ extremes is analyzed in Figure 4 as it was for B values. In panel 4(a), the model fits the observations within the confidence interval. Again in panel 4(b), the model fits the data well at lower $\frac{dB}{dt}$, and this is also true from examination of the QQ plot in panel 4(c). In each of the assessment figures, the GEVD model tends to fit $\frac{dB}{dt}$ data better than it did for B data, except for one outlier at high $\frac{dB}{dt}$.

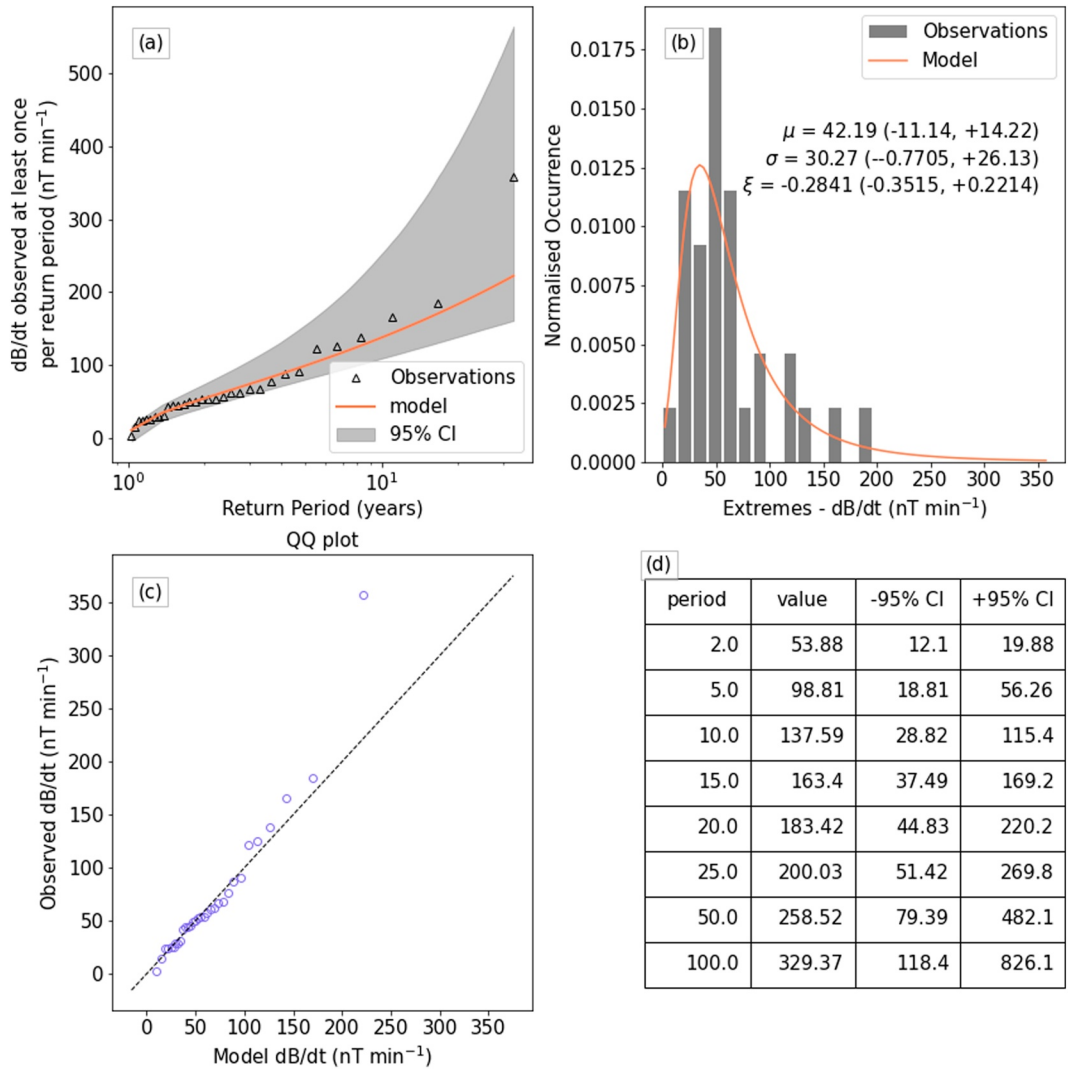

(d)

period	value	-95% CI	+95% CI
2.0	53.88	12.1	19.88
5.0	98.81	18.81	56.26
10.0	137.59	28.82	115.4
15.0	163.4	37.49	169.2
20.0	183.42	44.83	220.2
25.0	200.03	51.42	269.8
50.0	258.52	79.39	482.1
100.0	329.37	118.4	826.1

Figure 4. Extreme value analysis for $\frac{dB}{dt}$. (a) Observed extremes as a function of their calculated return periods (triangles), modeled extremes as a function of return period (orange line) with 95% confidence interval (gray shade). (b) Normalized distributions of the detected $\frac{dB}{dt}$ extremes (gray bars) and the fitted Generalized Extreme Value Distribution model (orange line), with the fitted parameters defined as for Equation 3 noted in the top right and the width of a 95% confidence interval. (c) Quantile-quantile plot comparing the distributions of the modeled (x) and observed (y) extremes. (d) Return values ("value") as a function of return period ("period" in years), with the width of a 95% confidence interval as an errorbar.

The return values for $\frac{dB}{dt}$ are presented with 95% confidence intervals in the table in panel 4(d). For example, Valentia $\frac{dB}{dt}$ observations are likely to exceed 183.42 nT min^{-1} (95% CI: −44.83, +220.2) at least once in a 20 year period.

4. Contributions to Extreme Values

In this section, the values observed at Valentia during geomagnetic storms, substorms and SCs will be compared with the return values extracted from the EVA. The values of B recorded at Valentia during different phases of storms, substorms and SCs are recorded in Figure 5 (an equivalent plot for $\frac{dB}{dt}$ is presented in Figure 6). For

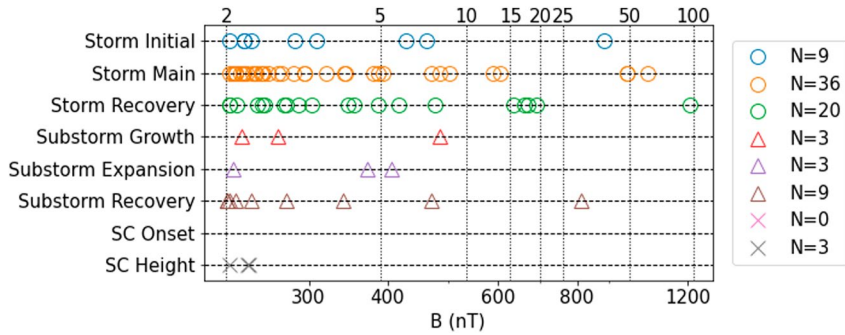

Figure 5. Valentia B values during different event phases. For storms, the maximum value in the labeled phase of each M.-T. Walach and Grocott (2019) storm between 1991 and 2021. For substorms, the maximum value in each phase (where recovery phase is the 30 min following recovery start time) for Forsyth et al. (2015) SOPHIE substorms between 1996 and 2014. Finally, for sudden commencements (SCs), the onset value is the maximum value between onset time and the end of the SC increase, whereas the height value is the maximum value from the end of the SC increase to 10 min afterward. Only B measurements greater than the 2 years return value of 222.0 nT are plotted. Vertical lines indicate 2, 5, 10, 15, 20, 25, 50, and 100 years return values. Number of points for each category is recorded in the legend. Horizontal axis is in log scale.

storms, the maximum value during initial, main and recovery phase is calculated using the M.-T. Walach and Grocott (2019) storm list. Similarly for substorms, the maximum value during growth, expansion and recovery phase (where these phases are defined in Section 2) from the Forsyth et al. (2015) SOPHIE substorm list. Finally, for SCs, the maximum recorded value for the period between onset and height of the step change ("onset") and the height of the step change and the 10 min that follow ("height") are extracted. For all three event types, only observations which equal or exceed the 2 years return value for B or $\frac{dB}{dt}$ are plotted.

For B values presented in Figure 5, storms contribute a larger number of observations above the 2 years return value than substorms or SCs (notably there are no SC onset observations that exceed the 2 years return value). This is particularly interesting given that there are many more substorms observed than storms: only 314 storms, but over 26,000 substorms. Despite this, all three phases of storms and substorms contribute to high B observations. SC onset does not contribute to high B observations, perhaps since this is the start of the step change that forms an SC, and so the horizontal component of the magnetic field will be at its lowest for this event. Conversely, at SC height, where the magnetic field should be the highest (within the SC time frame), there are three observations above the 2 years return value.

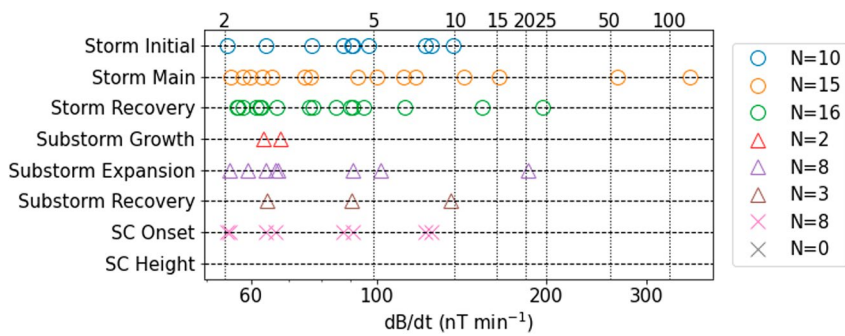

Figure 6. Valentia $\frac{dB}{dt}$ values during different event phases. For storms, the maximum value in the labeled phase of each M.-T. Walach and Grocott (2019) storm between 1991 and 2021. For substorms, the maximum value in each phase (where recovery phase is the 30 min following recovery start time) for Forsyth et al. (2015) SOPHIE substorms between 1996 and 2014. Finally, for sudden commencements (SCs), the onset value is the maximum value between onset time and the end of the SC increase, whereas the height value is the maximum value from the end of the SC increase to 10 min afterward. Only $\frac{dB}{dt}$ measurements greater than the 2 years return value of 53.88 nT min^{-1} are plotted. Vertical lines indicate 2, 5, 10, 15, 20, 25, 50, and 100 years return values. Number of points for each category is recorded in the legend. Horizontal axis is in log scale.

Table 1
Fit Parameters and Return Values for Extreme Value Analysis Analysis of Various Interplanetary Magnetic Field, Solar Wind Characteristics and Geomagnetic Indices; Left Hand Column Denotes the Parameter

Parameter	Distribution	μ	σ	ξ	2	5	10	15	20	25
B_{TOTAL} (nT)	Gumbel	30.8	11.5	0.00	35.0	48.0	57.0	61.0	65.0	67.0
$B_Y > 0$ (nT)	Gumbel	24.8	8.8	0.00	28.0	38.0	45.0	48.0	51.0	53.0
$B_Y < 0$ (nT)	Gumbel	−7.4	7.6	0.00	−26.0	−35.0	−41.0	−44.0	−46.0	−48.0
$B_Z > 0$ (nT)	Gumbel	23.8	8.3	0.00	27.0	36.0	42.0	46.0	48.0	50.0
$B_Z < 0$ (nT)	Gumbel	−5.5	9.3	0.00	−28.0	−39.0	−46.0	−50.0	−52.0	−55.0
V_{SW} (km s^{-1})	Gumbel	833.5	96.5	0.00	869.0	978.0	1051.0	1091.0	1120.0	1142.0
P_{SW} (nPa)	GEVD	28.5	12.0	−0.37	33.0	52.0	70.0	83.0	93.0	102.0
AE (nT)	Gumbel	2345.4	640.7	0.00	2580.0	3306.0	3787.0	4059.0	4249.0	4395.0
AU (nT)	Gumbel	819.1	313.8	0.00	934.0	1290.0	1525.0	1658.0	1751.0	1823.0
AL (nT)	Gumbel	−247.6	646.6	0.00	−2339.0	−3072.0	−3558.0	−3831.0	−4023.0	−4171.0
SYM-H (nT)	Gumbel	137.0	91.4	0.00	−181.0	−284.0	−353.0	−391.0	−419.0	−439.0
$PC_N > 0$ (mV m^{-1})	GEVD	13.8	5.2	−0.25	16.0	23.0	30.0	34.0	37.0	40.0
$PC_N < 0$ (mV m^{-1})	GEVD	1.9	5.1	−0.55	−10.0	−20.0	−31.0	−39.0	−46.0	−53.0

Note. Distribution indicates whether the GEVD or Gumbel distribution was fitted; both are fitted using MCMC as for B and $\frac{dB}{dt}$. μ, σ, and ξ denote the free parameters in the fitting. Columns 2, 5, 10, 15, 20, and 25 denote the return values for the titular return period in years. It is important to note that where the distribution used is Gumbel, ξ is fixed at exactly zero.

Figure 6 shows the $\frac{dB}{dt}$ values recorded by Valentia during the storms, substorms and SCs which equal or exceed the 2 year return value. Again, all three phases of storms and substorms contribute to these unusual $\frac{dB}{dt}$ values, while storms however contribute more high $\frac{dB}{dt}$ than substorms. Unlike for B, SC onset rather than height contribute to high $\frac{dB}{dt}$ values. This is likely as the onset period represents the beginning of the step change, so will contain high values of $\frac{dB}{dt}$ due to the nature of the change. The height portion comes from values following the step change, so may not contribute to high $\frac{dB}{dt}$ values. It is important to note at this point that ULF waves or related field-line resonances may contribute to high $\frac{dB}{dt}$ values, but the minute resolution of Valentia data is not fine enough to capture these rapid changes; further investigation with higher resolution data is necessary to determine to what extent wave activity contributes to high $\frac{dB}{dt}$ values.

An interesting point to consider in this analysis is that substorms may occur during storms, and so some of the B and $\frac{dB}{dt}$ values in the storm and substorm phases may come from similar intervals. However, the aim of this analysis was to characterize the contributions different events make to extreme values, and separating events into storms with/without substorms is out of the scope of this study.

Finally, the EVA technique (as applied to B and $\frac{dB}{dt}$) is applied to various IMF, solar wind characteristics and geomagnetic indices, using data between 1991 and 2021 inclusive. These results are summarized in Table 1. Rather than an in depth analysis as for B and $\frac{dB}{dt}$, for brevity the distribution and fit parameters are presented, along with the return values for 2, 5, 10, 15, 20, and 25 years. These return values will be used to assess the rarity of the conditions that generate the extreme B value presented in Figure 1. Guided by the distributions presented by Fogg et al. (2022), the EVA is run over block minima (i.e., negative maxima) for AL and SYM-H. This also links to negative signatures in AL generated by substorms, and negative signatures in SYM-H relating to geomagnetic storms. Finally, it is important to note that solar cycle variations in solar wind, IMF and geomagnetic indices have not been removed in this analysis: the purpose of this analysis is to assess the rarity of observations in Figure 1, and hence which parameters are driving the observed B extreme.

Note that EVA was applied separately to minima and maxima for B_Y, B_Z, or PC_N as these parameters are roughly equally likely to be positive or negative (following on from the distributions presented by Fogg et al. (2022)), and the geophysical meaning of these different signs is significant. For example, positive PC_N indicates Dungey driven dual cell convection, whereas negative PC_N may indicate reverse convection or a severe asymmetry in the convection pattern. Although different signs of B_Y relate to opposite asymmetries in magnetospheric and iono-

spheric signatures, some magnitude of either sign may increase energy input from the solar wind (e.g., Grocott et al., 2003; Grocott et al., 2004, 2008); however interpretation of, for example, the return period of the magnitude of B_Y would be non-trivial. Finally, for IMF B_Z, the difference between positive and negative represents a fundamental difference in the energy transfer between the solar wind and magnetosphere - the difference between a Dungey cycle-driven magnetosphere prone to storms and substorms, and a magnetosphere moving toward a more closed state (e.g., Milan et al., 2020; Milan et al., 2022).

In the example presented in Figure 1, B_{TOTAL} is fairly steady around 50 nT throughout the interval, driven by a dominant IMF B_Y of magnitude approximately 45 nT, and B_Z of approximately -50 to -10 nT. According to the return values presented in Table 1 this is between a 5- and 10-year event in B_{TOTAL}, and the interval starts with an approximately 15-year event in $B_Z < 0$, and continues with a 15- to 20-year event in $B_Y > 0$. The solar wind flow speed is greater than 1050 km s^{-1} at the time of the B extreme, between a 10- and 15-year event according to Table 1. The flow pressure varies between 10 and 30 nPa through the presented interval surrounding the B maximum. The 2-year return value of flow pressure is 33 nPa, so since the pressure is often below this value it is likely not driving the extreme observations in B.

Both AL and AE do not reach the their 2-year return values in the presented interval, observed at around -500 and $+1{,}000$ nT respectively. AU however exceeds the 2-year return value, suggesting that perhaps this interval is dominated by moderate-strong dayside driving, rather than nightside substorm driving characteristic of AL. Finally, in Figure 1, SYM-H is around -300 nT, between the 5- and 10-year return values, and far below the quiet threshold (M.-T. Walach & Grocott, 2019). Bergin et al. (2023) performed EVA on Dst, SYM-H and SMR, and the calculated 5- and 10-year return values are within their confidence intervals for the same return values (see Table 2 of Bergin et al. (2023)). At the onset of the extreme in Figure 1b, PC_N exhibits a value of around 15 mV m^{-1}, only a 2-year event according to Table 1.

In the B extreme presented in Figure 1, IMF B_{TOTAL}, V_{SW}, and SYM-H are exhibiting between 5- and 10-year values. The beginning of the interval is driven by a 15-year event in B_Z and B_Y. Considering the lack of characteristic substorm signatures in AL, and a long period of strong southward IMF, results from Table 1 suggest the B extreme is driven by a once in 5/10-year geomagnetic storm, incorporating strong solar wind driving in particular from V_{SW}, B_Y, and B_Z.

5. Conclusion

Investigation of space weather effects on Ireland is at an early stage when compared with other geographical areas, with the majority of this research utilizing the MagIE network of magnetometers. In this study, extreme events at the MagIE station at Valentia have been identified as the peak value observed in a calendar year. A GEVD model was fitted to these data via MCMC fitting, and from this model return values at given return periods are extracted. This process was repeated for both the horizontal component of the magnetic field, B, and its time derivative, $\frac{dB}{dt}$. Understanding the return values at Valentia provides a window onto space weather effects at Ireland, which is becoming increasingly important as the world moves toward a more technologically dependent society.

Additionally, the MLT distribution of the detected extremes was examined. As Ireland moves from day to night, the Valentia magnetometer rotates in and out of view of different regions of the magnetosphere, which can be dominated by different phenomena. More extremes were detected at premidnight MLTs, linking back to the dominance of substorm dynamics in the premidnight sector, and the dramatic bay-like features observed in magnetometer observations. Also presented in this study was an extreme in B, in a period with a strong B_{TOTAL}, and dominated by a 5- to 10-year storm and 15-year driving in the IMF.

The key results are summarized below:

1. There is a local time dependence to the distribution of B extremes at Valentia observatory. More B extremes are observed in the premidnight sector.
2. Return values of B and $\frac{dB}{dt}$ for Valentia observatory are predicted, and errors on these values are smaller at the lower end of extreme values, where the GEVD model fits the distribution best.
3. A 1 in 50-year event in B $\left(\frac{dB}{dt}\right)$ at Valentia observatory has a magnitude of 971.0 nT (258.52 nT min^{-1}).

4. A 1 in 100-year event in B $\left(\frac{dB}{dt}\right)$ at Valentia observatory has a magnitude of 1224.0 nT (329.37 nT min^{-1}).
5. Storms contribute more to extremes in both B and $\frac{dB}{dt}$ despite there being many fewer storms than substorms.
6. Return values on various solar wind, IMF and geomagnetic indices are predicted and presented in Table 1.

As presented in the key results above, 1 in 50-year and 1 in 100-year event magnitudes have been estimated for B and $\frac{dB}{dt}$ observations at Valentia Observatory. These are the type of event timescales that national government bodies seek to plan for, so it is important to estimate them. Since 50 and 100 years are beyond the extent of the available minute resolution data, the errors on these calculated return values are large, but they will give an indication of the extent of the magnetic field disturbance over Ireland in such extreme events.

To add context to the results of this paper, the observations at Valentia during the famous St Patrick's day storm on 17 March 2015 (e.g., Zhang et al., 2017) are considered. The maximum B observed at Valentia on this date was 303.3 nT at 23:24 UT, a magnitude comparable to H variations observed by for example, Nava et al. (2016) at low latitudes, and larger magnitude than high and polar latitude observations by for example, Marsal et al. (2016). However, it is a low magnitude observation compared to other extremes observed within the Valentia lifetime, and has a calculated return period of a 1 in 2-year event. The same is true for $\frac{dB}{dt}$: a maximum observed at 17:39 UT of 72.8 nT min^{-1}, another 1 in 2-year event. So although the global implications of this event were significant, causing for example, issues for GPS systems (e.g., Jin & Oksavik, 2018), the implications for Ireland were not as dramatic as other events observed in the lifetime of Valentia. This is an important point, highlighting that global space weather events do not necessarily result in extreme local space weather implications.

Data Availability Statement

Data from Valentia MagIE station was obtained via the SuperMAG archive (J. W. Gjerleov & SuperMAG Collaborators, 2023). SuperMAG is made possible by the generous funding provided by the National Science Foundation (NSF) and National Aeronautics and Space Administration (NASA). We gratefully acknowledge: NSF ATM-0646323, NSF AGS-1003580, NASA NNX08AM32G S03. We gratefully acknowledge the SuperMAG collaborators (Gjerlov, 2012). SuperMAG indices SME/SMU/SML (Newell & Gjerloev, 2011) and SMR (Newell & Gjerloev, 2012) were obtained from J. W. Gjerleov and SuperMAG Collaborators (2023). We gratefully acknowledge use of NASA/GSFC's Space Physics Data Facility's OMNIWeb service, and OMNI data (N. Papitashvili, 2023). The AE and SYM-H indices used in this paper were provided by the WDC for Geomagnetism, Kyoto via OMNIWeb (N. Papitashvili, 2023). PC(N) index was provided by World Data Center for Geomagnetism, Copenhagen via OMNIWeb. Sunspot data from the World Data Center SILSO (Sunspot Index and Long-term Solar Observations (SILSO) at the Royal Observatory of Belgium, 2020), Royal Observatory of Belgium, Brussels. A subset of M.-T. Walach and Grocott (2019) storms are available in the Supporting Information S1, and those used in this manuscript are available from M. Walach (2023). The SOPHIE substorm list is available in the Supporting Information of Forsyth et al. (2015). The sudden commencement event list used in this paper was compiled by Observatori de l'Ebre (2020). The authors gratefully acknowledge the use of the pyextremes python package (Bocharov, 2023), and fruitful conversations with its author George Bocharov. The authors also gratefully acknowledge the use of the emcee python package by Foreman-Mackey et al. (2013).

Acknowledgments
ARF's work was supported by Irish Research Council Government of Ireland Postdoctoral Fellowship GOIPD/2022/782. CMJ's work was supported by the Science Foundation Ireland Grant 18/FRL/6199. JM-L was supported by the Irish Research Council. AWS was supported by NERC Independent Research Fellowship NE/W009129/1. MTW was supported by the UKRI Natural Environment Research Council Grant NE/T000937/1. ML is support by the UK Science, Technology and Facilities Council grant ST/W00089X/1. JEW was supported by a CNES postdoctoral fellowship.

References

Akaike, H. (1974). A new look at the statistical model identification. *IEEE Transactions on Automatic Control*, *19*(6), 716–723. https://doi.org/10.1109/TAC.1974.1100705

Araki, T. (1994). A physical model of the geomagnetic sudden commencement. *Geophysical Monograph*, *81*, 183–200. https://doi.org/10.1029/GM081p0183

Bergin, A., Chapman, S. C., & Gjerloev, J. W. (2020). AE, Dst, and their SuperMAG counterparts: The effect of improved spatial resolution in geomagnetic indices. *Journal of Geophysical Research: Space Physics*, *125*(5), e2020JA027828. https://doi.org/10.1029/2020JA027828

Bergin, A., Chapman, S. C., Watkins, N. W., Moloney, N. R., & Gjerloev, J. W. (2023). Extreme event statistics in Dst, SYM-H, and SMR geomagnetic indices. *Space Weather*, *21*(3), e2022SW003304. https://doi.org/10.1029/2022SW003304

Blake, S. P., Gallagher, P. T., Campanyà, J., Hogg, C., Beggan, C., Thomson, A. W. P., et al. (2018). A detailed model of the Irish high voltage power network for simulating GICs. *Space Weather*, *16*(11), 1770–1783. https://doi.org/10.1029/2018SW001926

Blake, S. P., Gallagher, P. T., McCauley, J., Jones, A. G., Hogg, C., Campanya, J., et al. (2016). Geomagnetically induced currents in the Irish power network during geomagnetic storms. *Space Weather*, *14*(12), 1136–1154. https://doi.org/10.1002/2016SW001534

Bocharov, G. (2023). pyextremes: Extreme value analysis (EVA) in python. Retrieved from https://github.com/georgebv/pyextremes

Bolduc, L. (2002). GIC observations and studies in the Hydro-Québec power system. *Journal of Atmospheric and Solar-Terrestrial Physics*, *64*(16), 1793–1802. https://doi.org/10.1016/S1364-6826(02)00128-1

Bristow, W. A., & Jensen, P. (2007). A superposed epoch study of SuperDARN convection observations during substorms. *Journal of Geophysical Research*, *112*(A6), A06232. https://doi.org/10.1029/2006JA012049

Bristow, W. A., Otto, A., & Lummerzheim, D. (2001). Substorm convection patterns observed by the super dual auroral radar network. *Journal of Geophysical Research*, *106*(A11), 24593–24609. https://doi.org/10.1029/2001JA000117

Bristow, W. A., Sofko, G. J., Stenbaek-Nielsen, H. C., Wei, S., Lummerzheim, D., & Otto, A. (2003). Detailed analysis of substorm observations using SuperDARN, UVI, ground-based magnetometers, and all-sky imagers. *Journal of Geophysical Research*, *108*(A3), 1124. https://doi.org/10.1029/2002JA009242

Campanyà, J., Gallagher, P. T., Blake, S. P., Gibbs, M., Jackson, D., Beggan, C. D., et al. (2019). Modeling geoelectric fields in Ireland and the UK for space weather. *Space Weather*, *17*(2), 216–237. https://doi.org/10.1029/2018SW001999

Chapman, S. C., McIntosh, S. W., Leamon, R. J., & Watkins, N. W. (2020). Quantifying the solar cycle modulation of extreme space weather. *Geophysical Research Letters*, *47*(11), e2020GL087795. https://doi.org/10.1029/2020GL087795

Coles, S. (2001). *An introduction to statistical modeling of extreme values*. Springer.

Davis, T. N., & Sugiura, M. (1966). Auroral electrojet activity index AE and its universal time variations. *Journal of Geophysical Research*, *71*(3), 785–801. https://doi.org/10.1029/JZ071i003p00785

Elvidge, S. (2020). Estimating the occurrence of geomagnetic activity using the Hilbert-Huang transform and extreme value theory. *Space Weather*, *17*(8), e2020SW002513. https://doi.org/10.1029/2020SW002513

Fang, T.-W., Kubaryk, A., Goldstein, D., Li, Z., Fuller-Rowell, T., Millward, G., et al. (2022). Space weather environment during the SpaceX Starlink satellite loss in February 2022. *Space Weather*, *20*(11), e2022SW003193. https://doi.org/10.1029/2022SW003193

Finkel, J., Gerber, E. P., Abbot, D. S., & Weare, J. (2023). Revealing the statistics of extreme events hidden in short weather forecast data. *AGU Advances*, *4*(2), e2023AV000881. https://doi.org/10.1029/2023AV000881

Fogg, A. R. (2021). SuperDARN observations of high latitude electrodynamics in the terrestrial ionosphere (Doctoral dissertation). University of Leicester School of Physics and Astronomy. https://doi.org/10.25392/leicester.data.16621912.v1

Fogg, A. R., Jackman, C. M., Waters, J. E., Bonnin, X., Lamy, L., Cecconi, B., et al. (2022). Wind/WAVES observations of auroral kilometric radiation: Automated burst detection and terrestrial solar wind—Magnetosphere coupling effects. *Journal of Geophysical Research: Space Physics*, *127*(5), e2021JA030209. https://doi.org/10.1029/2021JA030209

Fogg, A. R., Lester, M., Yeoman, T. K., Carter, J. A., Milan, S. E., Sangha, H. K., et al. (2023). Multi-instrument observations of the effects of a solar wind pressure pulse on the high latitude ionosphere: A detailed case study of a geomagnetic sudden impulse. *Journal of Geophysical Research: Space Physics*, *128*(3), e2022JA031136. https://doi.org/10.1029/2022JA031136

Foreman-Mackey, D., Hogg, D. W., Lang, D., & Goodman, J. (2013). emcee: The MCMC Hammer. *Publications of the Astronomical Society of the Pacific*, *125*(925), 306–312. https://doi.org/10.1086/670067

Forsyth, C., Rae, I. J., Coxon, J. C., Freeman, M. P., Jackman, C. M., Gjerloev, J., & Fazakerley, A. N. (2015). A new technique for determining substorm onsets and phases from indices of the electrojet (SOPHIE). *Journal of Geophysical Research: Space Physics*, *120*(12), 10592–10606. https://doi.org/10.1002/2015JA021343

Freeman, M. P., Forsyth, C., & Rae, I. J. (2019). The influence of substorms on extreme rates of change of the surface horizontal magnetic field in the United Kingdom. *Space Weather*, *17*(6), 827–844. https://doi.org/10.1029/2018SW002148

Gillies, D. M., St. Maurice, J. P., McWilliams, K. A., & Milan, S. (2012). Global-scale observations of ionospheric convection variation in response to sudden increases in the solar wind pressure. *Journal of Geophysical Research*, *117*(A4), A04209. https://doi.org/10.1029/2011JA017255

Gjerleov, J. W., & SuperMAG Collaborators. (2023). SuperMAG data [Dataset]. SuperMAG Collaborators. Retrieved from https://supermag.jhuapl.edu/

Gjerlov, J. W. (2012). The SuperMAG data processing technique. *Journal of Geophysical Research*, A09213. https://doi.org/10.1029/2012JA017683

Grocott, A., Badman, S. V., Cowley, S. W. H., Yeoman, T. K., & Cripps, P. J. (2004). The influence of IMF By on the nature of the nightside high-latitude ionospheric flow during intervals of positive IMF Bz. *Annales Geophysicae*, *22*(5), 1755–1764. https://doi.org/10.5194/angeo-22-1755-2004

Grocott, A., Cowley, S. W. H., & Sigwarth, J. B. (2003). Ionospheric flow during extended intervals of northward but B_Y-dominated IMF. *Annales Geophysicae*, *21*(2), 509–538. https://doi.org/10.5194/angeo-21-509-2003

Grocott, A., Milan, S. E., & Yeoman, T. K. (2008). Interplanetary magnetic field control of fast azimuthal flows in the nightside high-latitude ionosphere. *Geophysical Research Letters*, *35*(8), L08102. https://doi.org/10.1029/2008GL033545

HM Government Cabinet Office (2020). National risk register 2020. Retrieved from https://www.gov.uk/government/publications/national-risk-register-2020

Hori, T., Shinbori, A., Fujita, S., & Nishitani, N. (2015). IMF-By dependence of transient ionospheric flow perturbation associated with sudden impulses: SuperDARN observations. *Earth Planets and Space*, *67*(190), 190. https://doi.org/10.1186/s40623-015-0360-6

Hutchinson, J. A., Wright, D. M., & Milan, S. E. (2011). Geomagnetic storms over the last solar cycle: A superposed epoch analysis. *Journal of Geophysical Research*, *116*(A9), A09211. https://doi.org/10.1029/2011JA016463

Hutchinson, J. A., Wright, D. M., Milan, S. E., Grocott, A., & Boakes, P. D. (2011). A new way to study geomagnetic storms. *Astronomy and Geophysics*, *52*(4), 4.20–4.23. https://doi.org/10.1111/j.1468-4004.2011.52420.x

Iyemori, T. (1990). Storm-time magnetospheric currents inferred from mid-latitude geomagnetic field variations. *Journal of Geomagnetism and Geoelectricity*, *42*(11), 1249–1265. https://doi.org/10.5636/jgg.42.1249

James, M. K., Yeoman, T. K., Jones, P., Sandhu, J. K., & Goldstein, J. (2021). The scalable plasma ion composition and electron density (SPICED) model for Earth's inner magnetosphere. *Journal of Geophysical Research: Space Physics*, *126*(9), e2021JA029565. https://doi.org/10.1029/2021JA029565

Jin, Y., & Oksavik, K. (2018). GPS scintillations and losses of signal lock at high latitudes during the 2015 St. Patrick's Day Storm. *Journal of Geophysical Research: Space Physics*, *123*(9), 7943–7957. https://doi.org/10.1029/2018JA025933

King, J. H., & Papitashvili, N. E. (2005). Solar wind spatial scales in and comparisons of hourly Wind and ACE plasma and magnetic field data. *Journal of Geophysical Research*, *110*(A2), A02104. https://doi.org/10.1029/2004JA010649

Koons, H. C. (2001). Statistical analysis of extreme values in space science. *Journal of Geophysical Research*, *106*(A6), 10915–10921. https://doi.org/10.1029/2000JA000234

Love, J. J., & Chulliat, A. (2013). An international network of magnetic observatories. *Eos, Transactions, American Geophysical Union*, *94*(42), 373–374. https://doi.org/10.1002/2013EO420001

Malone-Leigh, J., Campanyà, J., Gallagher, P. T., Neukirch, M., Hogg, C., & Hoggson, J. (2023). Nowcasting geoelectric fields in Ireland using magnetotelluric transfer functions. *Journal of Space Weather and Space Climate*, *13*, 6. https://doi.org/10.1051/swsc/2023004

Marangio, P., Christodoulou, V., Filgueira, R., Rogers, H. F., & Beggan, C. D. (2020). Automatic detection of ionospheric Alfven resonances in magnetic spectrograms using u-net. *Computers & Geosciences*, *145*, 104598. https://doi.org/10.1016/j.cageo.2020.104598

Marsal, S., Torta, J. M., Segarra, A., & Araki, T. (2016). Use of spherical elementary currents to map the polar current systems associated with the geomagnetic sudden commencements on 2013 and 2015 St. Patrick's Day storms. *Journal of Geophysical Research: Space Physics*, *122*(1), 194–211. https://doi.org/10.1002/2016JA023166

McPherron, R. L. (1970). Growth phase of magnetospheric substorms. *Journal of Geophysical Research*, *75*(28), 5592–5599. https://doi.org/10.1029/JA075i028p05592

McPherron, R. L. (1995). Magnetospheric dynamics. In M. G. Kivelson & C. T. Russell (Eds.), *Introduction to space physics* (pp. 400–458). Cambridge University Press.

Milan, S. E., Bower, G. E., Carter, J. A., Paxton, L. J., Anderson, B. J., & Hairston, M. R. (2022). Lobe reconnection and cusp-aligned auroral arcs. *Journal of Geophysical Research: Space Physics*, *127*(6), e2021JA030089. https://doi.org/10.1029/2021JA030089

Milan, S. E., Carter, J. A., Bower, G. E., Imber, S. M., Paxton, L. J., Anderson, B. J., et al. (2020). Dual-lobe reconnection and horse-collar auroras. *Journal of Geophysical Research: Space Physics*, *125*(10), e2020JA028567. https://doi.org/10.1029/2020JA028567

Nava, B., Rodríguez-Zuluaga, J., Alazo-Cuartas, K., Kashcheyev, A., Migoya-Orué, Y., Radicella, S. M., et al. (2016). Middle- and low-latitude ionosphere response to 2015 St Patrick's Day geomagnetic storm. *Journal of Geophysical Research: Space Physics*, *121*(4), 3421–3438. https://doi.org/10.1002/2015JA022299

Newell, P. T., & Gjerloev, J. W. (2011). Evaluation of SuperMAG auroral electrojet indices as indicators of substorms and auroral power. *Journal of Geophysical Research*, *116*(A12), A12211. https://doi.org/10.1029/2011JA016779

Newell, P. T., & Gjerloev, J. W. (2012). SuperMAG-based partial ring current indices. *Journal of Geophysical Research*, *117*(A5), A05215. https://doi.org/10.1029/2012JA017586

Nishimura, Y., Lyons, L. R., Gabrielse, C., Sivadas, N., Donovan, E. F., Varney, R. H., et al. (2020). Extreme magnetosphere-ionosphere-thermosphere responsews to the 5 April 2010 supersubstorm. *Journal of Geophysical Research: Space Physics*, *125*(4), e2019JA027654. https://doi.org/10.1029/2019JA027654

Observatori de l'Ebre. (2020). International service on rapid magnetic variations. Retrieved from http://www.obsebre.es/en/rapid

Oliveira, D. M., Hartinger, M. D., Xi, Z., Zesta, E., Pilipenko, V. A., Giles, B. L., & Silveira, M. V. D. (2020). Interplanetary shock impact angles control magnetospheric ULF wave activity: Wave amplitude, frequency, power spectra. *Geophysical Research Letters*, *47*(24), e2020GL090857. https://doi.org/10.1029/2020GL090857

Orr, L., Grocott, A., Walach, M.-T., Chisham, G., Freeman, M. P., Lam, M. M., & Shore, R. M. (2023). A quantitative comparison of high latitude electric field models during a large geomagnetic storm. *Space Weather*, *21*(1), e2022SW003301. https://doi.org/10.1029/2022SW003301

Papitashvili, N. (2023). Omniweb plus [Dataset]. GSFC. Retrieved from https://omniweb.gsfc.nasa.gov/hw.html

Riley, P., & Love, J. J. (2017). Extreme geomagnetic storms: Probabilistic forecasts and their uncertainties. *Space Weather*, *15*(1), 53–64. https://doi.org/10.1002/2016SW001470

Rogers, N. C., Wild, J. A., Eastoe, E. F., Gjerloev, J. W., & Thomson, A. W. P. (2020). A global climatological model of extreme geomagnetic field fluctuations. *Journal of Space Weather and Space Climate*, *10*(5), 5. https://doi.org/10.1051/swsc/2020008

Sandhu, J. K., Rae, I. J., Wygant, J. R., Breneman, A. W., Tian, S., Watt, C. E. J., et al. (2021). Ulf wave driven radial diffusion during geomagnetic storms: A statistical analysis of van Allen probes observations. *Journal of Geophysical Research: Space Physics*, *126*(4), e2020JA029024. https://doi.org/10.1029/2020JA029024

Sangha, H., Milan, S. E., Carter, J. A., Fogg, A. R., Anderson, B. J., Korth, H., & Paxton, L. J. (2020). Bifurcated region 2 field-aligned currents associated with substorms. *Journal of Geophysical Research: Space Physics*, *125*(1), e2019JA027041. https://doi.org/10.1029/2019JA027041

Silbergleit, V. M. (1996). On the occurrence of geomagnetic storms with sudden commencements. *Journal of Geomagnetism and Geoelectricity*, *48*(7), 1011–1016. https://doi.org/10.5636/jgg.48.1011

Silbergleit, V. M. (1999). Forecast of the most geomagnetically disturbed days. *Earth Planets and Space*, *51*(1), 19–22. https://doi.org/10.1186/BF03352205

Siscoe, G. L. (1976). On the statistics of the largest geomagnetic storms per solar cycle. *Journal of Geophysical Research*, *81*(25), 4782–4784. https://doi.org/10.1029/JA081i025p04782

Smith, A. W., Forsyth, C., Rae, J., Rodger, C. J., & Freeman, M. P. (2021). The impact of sudden commencements on ground magnetic field variability: Immediate and delayed consequences. *Space Weather*, *19*(7), e2021SW002764. https://doi.org/10.1029/2021SW002764

Smith, A. W., Freeman, M. P., Rae, I. J., & Forsyth, C. (2019). The influence of sudden commencements on the rate of change of the surface horizontal magnetic field in the United Kingdom. *Space Weather*, *17*(11), 1605–1617. https://doi.org/10.1029/2019SW002281

Smith, A. W., Jackman, C. M., Frohmaier, C. M., Coxon, J. C., Slavin, J. A., & Fear, R. C. (2018). Evaluating single-spacecraft observations of planetary magnetotails with simple Monte Carlo simulations: 1. Spatial distributions of the neutral line. *Journal of Geophysical Research: Space Physics*, *123*(10), 10109–10123. https://doi.org/10.1029/2018JA025958

Stauning, P. (2013). The polar cap index: A critical review of methods and a new approach. *Journal of Geophysical Research: Space Physics*, *118*(8), 5021–5038. https://doi.org/10.1002/jgra.50462

Sunspot Index and Long-term Solar Observations (SILSO) at the Royal Observatory of Belgium. (2020). Sunspot index and long-term solar observations (SILSO): Sunspot number. Retrieved from http://www.sidc.be/silso/datafiles

Thomson, A. W. P., Dawson, E. B., & Reay, S. J. (2011). Quantifying extreme behaviour in geomagnetic activity. *Space Weather*, *9*(10), S10001. https://doi.org/10.1029/2011SW000696

Troshichev, O. A., & Andrezen, V. G. (1985). The relationship between interplanetary quantities and magnetic activity in the southern polar cap. *Planetary and Space Science*, *33*(4), 415–419. https://doi.org/10.1016/0032-0633(85)90086-8

Troshichev, O. A., Dmitrieva, N. P., & Kuznetsov, B. M. (1979). Polar cap magnetic activity as a signature of substorm development. *Planetary and Space Science*, *27*(3), 217–221. https://doi.org/10.1016/0032-0633(79)90063-1

Tsubouchi, K., & Omura, Y. (2007). Long-term occurrence probabilities of intense geomagnetic storm events. *Space Weather*, *5*(12), S12003. https://doi.org/10.1029/2007SW000329

Walach, M. (2023). Geomagnetic storm list 1981–2019. https://doi.org/10.17635/lancaster/researchdata/622

Walach, M.-T., & Grocott, A. (2019). SuperDARN observations during geomagnetic storms, geomagnetically active times and enhanced solar wind driving. *Journal of Geophysical Research: Space Physics*, *124*(7), 5828–5847. https://doi.org/10.1029/2019JA026816

Waters, J. E., Jackman, C. M., Whiter, D., Forsyth, C., Fogg, A. R., Lamy, L., et al. (2022). A perspective on substorm dynamics using 10 years of Auroral Kilometric Radiation observations from Wind. *Journal of Geophysical Researc: Space Physics*, *127*(9), 127. https://doi.org/10.1029/2022JA030449

Weimer, D. R., & King, J. H. (2008). Improved calculations of interplanetary magnetic field phase front angles and propagation time delays. *Journal of Geophysical Research*, *113*(A1), A01105. https://doi.org/10.1029/2007JA012452

Weimer, D. R., Ober, D. M., Maynard, N. C., Burke, W. J., Collier, M. R., McComas, D. J., et al. (2002). Variable time delays in the propagation of the interplanetary magnetic field. *Journal of Geophysical Research*, *107*(A8), SMP29-1–SMP29-15. https://doi.org/10.1029/2001JA009102

Weimer, D. R., Ober, D. M., Maynard, N. C., Collier, M. R., McComas, D. J., Ness, N. F., & Watermann, J. (2003). Predicting interplanetary magnetic field (IMF) propagation delay times using the minimum variance technique. *Journal of Geophysical Research*, *108*(A1), 1026. https://doi.org/10.1029/2002JA009405

Wharton, S. J., Rae, I. J., Sandhu, J. K., Walach, M.-T., Wright, D. M., & Yeoman, T. K. (2020). The changing eigenfrequency continuum during geomagnetic storms: Implications for plasma mass dynamics and ULF wave coupling. *Journal of Geophysical Research: Space Physics*, *125*(6), e2019JA027648. https://doi.org/10.1029/2019JA027648

World Data Center for Geomagnetism Kyoto, Nose, M., Iyemori, T., Sugiura, M., & Kamei, T. (2015). Geomagnetic AE index. https://doi.org/10.17593/15031-54800

Zhang, S. R., Zhang, Y., Wang, W., & Verkhoglyadova, O. P. (2017). Geosphace system responses to the St Patrick's Day storms in 2013 and 2015. *Journal of Geophysical Research: Space Physics*, *122*(6), 6901–6906. https://doi.org/10.1002/2017JA024232